

SUPER – A Framework for Sensitivity-based Uncertainty-aware Performance and Risk Assessment in Visual Inertial Odometry

Johannes A. Gaus¹, Daniel Häufle¹, and Woo-Jeong Baek²

Abstract— While many visual odometry (VO), visual-inertial odometry (VIO), and SLAM systems achieve high accuracy, the majority of existing methods miss to assess risks at runtime. This paper presents SUPER (Sensitivity-based Uncertainty-aware PErformance and Risk assessment) that is a generic and explainable framework that propagates uncertainties via sensitivities for real-time risk assessment in VIO. The scientific novelty lies in the derivation of a real-time risk indicator that is backend-agnostic and exploits the Schur complement blocks of the Gauss-Newton normal matrix to propagate uncertainties. Practically, the Schur complement captures the sensitivity that reflects the influence of the uncertainty on the risk occurrence. Our framework estimates risks on the basis of the residual magnitudes, geometric conditioning, and short horizon temporal trends without requiring ground truth knowledge. Our framework enables to reliably predict trajectory degradation 50 frames ahead with an improvement on 20% to the baseline. In addition, SUPER initiates a stop or relocation policy with 89.1% recall. The framework is backend agnostic and operates in real time with less than 0.2% additional CPU cost. Experiments show that SUPER provides consistent uncertainty estimates. A SLAM evaluation highlights the applicability to long horizon mapping.

I. INTRODUCTION

Optimizing the accuracy in motion estimation from cameras and inertial sensors has become routine for the robotics domain [1]–[5]. Yet, most modern visual odometry (VO), visual-inertial odometry (VIO), and SLAM systems do not provide an explicit measure of risks during operation. While the single best estimate of the pose is computed, a distinct measure indicating the reliability or stability of that estimate is missing. Hence, once conditions degrade due to blur, noise, low texture, or occlusion, risk signals are initiated after the accumulation of errors. As a consequence, countermeasures are triggered with significant delays [6]–[8]. In safety-critical settings and dynamic environments, this limitation can result in undesired hazards or even accidents [9], [10]. To address this problem, this manuscript introduces the framework SUPER for real-time risk assessment in VIO and SLAM. Specifically, SUPER builds on the safety definition provided by the International Organization for Standardization (ISO), where the risk corresponds to the inverse of safety. Accordingly, the risk is proportional to the occurrence probability of hazardous events [11]. Contending that the uncertainty quantification is one possibility to capture this

¹ Hertie Institute for Clinical Brain Research & Center for Integrative Neuroscience, University of Tübingen, Germany.

² Intelligent Process Automation and Robotics Lab (IPR), Karlsruhe Institute of Technology (KIT), Germany, Artificial Intelligence Institute (AIIS), Seoul National University, Republic of Korea.

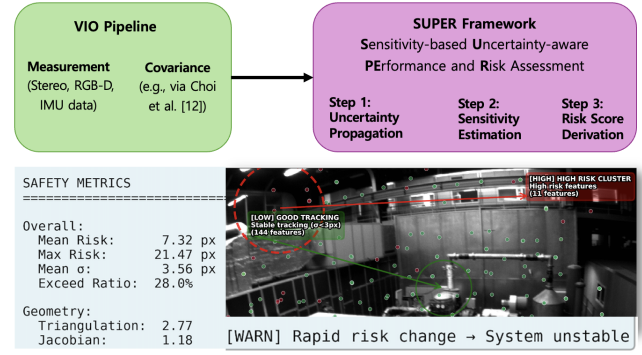


Fig. 1: Overview: SUPER leverages the Jacobians, residuals, and matrix structures that are formed during the optimization to derive one unified risk representation with real-time performance in VIO and SLAM systems.

occurrence probability, this manuscript suggests a sensitivity-based uncertainty-aware risk evaluation. The sensitivity is formalized by the Schur complement and reflects how the uncertainty impacts the system. In the majority of VIO and SLAM pipelines, runtime risk monitoring is limited to heuristic thresholds on residuals, feature counts, or filter covariances. The Jacobians and Schur complement computed during the optimization process are discarded after each update. Our key contribution lies in the derivation of a real-time risk indicator by exploiting these Jacobians and the Schur complement from the optimizer. More specifically, VIO and SLAM solvers like Gauss Newton and Levenberg Marquardt form Jacobians of reprojection residuals and assemble a Hessian matrix. SUPER refers to the corresponding Schur complement blocks to derive per feature world covariances in real-time without requiring additional optimization. Building upon the pipeline presented by Choi et al. in [12], our framework combines four complementary indicators: Propagated uncertainty, residual magnitude, geometric conditioning, and their temporal trends. A key advantage of our framework lies in its computational efficiency. To our knowledge, SUPER is the first explainable framework that evaluates risks at runtime on official safety standards by explicitly referring to uncertainty sources in VIO or SLAM via the sensitivity. Experiments on EuRoC, KITTI, and TUM VI show that SUPER produces clear warning signals with real time performance. A SLAM demonstration highlights the robustness in long horizon mapping. The remainder of this paper is structured as follows: Section II summarizes related works that develop methods for uncertainty-aware VIO and SLAM. By doing so, the novelty and scientific contributions of our manuscript are emphasized. Next, the

framework SUPER is derived in Section III by explaining the uncertainty propagation and the sensitivity-aware risk assessment. Afterward, the experimental setup is introduced in Section IV by specifying the evaluation metrics and baselines. Section V discusses the obtained results via in-depth analyses. The limitations are outlined in Section VI before summarizing the findings and future plans in Section VII.

II. RELATED WORK AND ISO STANDARDS

VO/VIO Systems. Early filter-based systems like MonoSLAM [1] and MSCKF [2] explicitly preserve covariances but suffered from linearization assumptions. Modern optimization-based pipelines (OKVIS [3] or LIO-SAM [13]) achieve high accuracy through bundle adjustment (BA) but typically discard Jacobians and Hessians after updates. In addition, works to retain probabilistic structures have been suggested. For example, ROVIO [8] couples photometric and probabilistic updates. On the other hand, Teed et al. in [5] implicitly capture uncertainty through recurrent tracking in DROID-SLAM. However, the interpretability of risk assessment techniques remains unaddressed.

Learning-based Uncertainty. Deep learning approaches (D3VO [7], DeepVO [14], differentiable filters [15], online calibration [12]) predict confidence efficiently but depend on training data. However, the authors miss to address the computation of analytic measures during operation for risk assessment that limits the applicability of the approaches for safety-critical environments. This manuscript aims to complement above works by deriving a risk assessment technique.

Risk-Aware Systems and ISO Standards. Uncertainty quantification is one possibility for risk assessment. Blackmore et al. showed that the consideration of uncertainties enables chance-constrained planning [16], probabilistic SLAM [9], and shared-autonomy systems [10]. In addition, the contribution in [17] demonstrates that incorporating the uncertainty in the robot control helps to detect risks in path planning algorithms. However, works that evaluate risks according to the official standards by the International Organization for Standardization (ISO) remain sparse. This paper refers to ISO 12100 that defines risks via the occurrence probability and severity of hazardous events. Prior works in ([18], [19], [20]) show that the propagated uncertainty enables to capture the occurrence probability of dangerous events. On this basis and referring to the derivative-based analysis [21], we propose a sensitivity-aware risk assessment framework.

Uncertainty in SLAM and Degeneracy Analysis. Marginal covariances can be recovered via GTSAM [22], iSAM2 [23], and g2o [24], but are typically computed offline due to cost. Information-theoretic metrics [25]–[27] characterize conditioning, while robustness studies [6] and learned models [28], [29] address noise statistically. Our indicators complement these by decomposing uncertainty into measurement noise, residual misfit, and geometric conditioning, remaining fully analytic and training-free. Most recent VO/VIO/SLAM

research has emphasized improving accuracy rather than quantifying how estimator uncertainty evolves during operation. Consequently, existing uncertainty methods can be categorized as follows: Perceptual confidence from deep networks, and local measurement–noise models from classical pipelines. Deep learning methods provide calibrated logits or heteroscedastic image–space variances, but reflect network belief instead of estimator sensitivity. Therefore, they do not consider the conditioning of the underlying BA problem. Classical covariance estimates and robust costs characterize local measurement noise, but miss to quantify how pixel perturbations amplify through triangulation, keyframe structure, or the Schur–complement coupling of a full estimator. Existing sensitivity analyses like the UAV-specific study of [30] perturb parameters offline to measure trajectory robustness, but lack real-time Jacobian-aware risk monitoring and cannot generate online warning signals before failures cascade. We address this gap by deriving SUPER, that exploits Jacobians and the Schur complement of the Gauss–Newton matrix to propagate pixel-space uncertainties through the optimizer in real time, thereby enabling the online risk-aware adaptation of parameters. The scientific contributions of this manuscript are twofold:

- 1) A sensitivity-aware uncertainty propagation method that extracts per-feature pixel covariances in real time from the Schur complement without additional computation.
- 2) A unified risk indicator that combines measurement noise, residual misfit, and geometric conditioning with temporal fluctuations.

Experiments on EuRoC, KITTI, and TUM-VI demonstrate that SUPER predicts near-future degradation 20% better than classical heuristics and enables reliable stop/relocalization policies.

III. THE FRAMEWORK SUPER

This section derives SUPER by showing how the Jacobians and the Gauss–Newton normal matrix from the backend optimization can serve to propagate the pixel level uncertainty and derive frame level risk indicators. Figure 2 depicts the components of SUPER.

A. First-Order Uncertainty Propagation

For a 3-D landmark $\mathbf{x} \in \mathbb{R}^3$ and projection $\pi : \mathbb{R}^3 \rightarrow \mathbb{R}^2$, small perturbations yield

$$\Sigma_{\text{pixel}} = J_\pi \Sigma_{\text{world}} J_\pi^\top, \quad (1)$$

where J_π is the projection Jacobian at the current linearization point. In incremental BA, residuals remain small, and Σ_{world} is obtained from the landmark block of the inverse normal matrix $(J^\top J + \lambda I)^{-1}$ at each Gauss–Newton update.

B. Schur Complement Extraction

The normal matrix from BA underlies a block structure

$$H = \begin{bmatrix} H_{pp} & H_{p\ell} \\ H_{\ell p} & H_{\ell\ell} \end{bmatrix}, \quad (2)$$

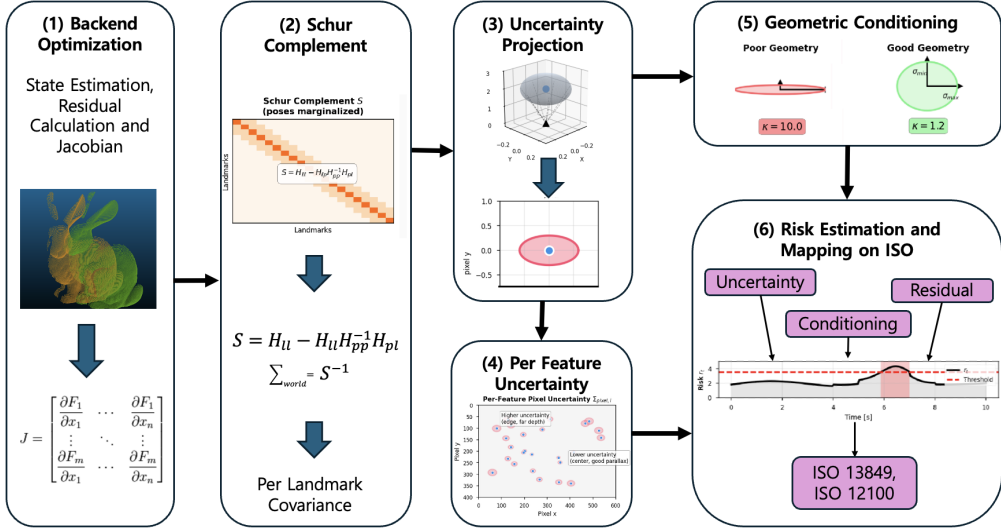


Fig. 2: **Schematic overview of SUPER.** (1) Backend optimization provides state estimates with residuals and Jacobians that form the normal matrix. (2) The Schur complement marginalizes poses and yields per landmark covariance. (3) Each covariance is projected into the pixel space to obtain per feature uncertainty. (4) Aggregating all pixel level covariances produces a dense map of feature uncertainties across the image. (5) Geometric conditioning is computed from the shape of each pixel covariance, revealing how viewing geometry affects estimation quality. (6) Uncertainty, residuals, and conditioning are combined into a risk score and mapped to ISO standards.

where H_{pp} contains pose-pose blocks and $H_{\ell\ell}$ landmark-landmark blocks. To marginalize out poses and obtain per-landmark covariances that properly account for pose-landmark coupling, the Schur complement

$$S = H_{\ell\ell} - H_{\ell p} H_{pp}^{-1} H_{p\ell}, \quad (3)$$

that modern solvers (Ceres [31], g2o [24], GTSAM [22]) compute with the linear solver for computational efficiency [32] is introduced. Per-landmark world covariances are given by

$$\Sigma_{\text{world},i} \approx S_{ii}^{-1}, \quad (4)$$

where S_{ii} is the 3×3 block for landmark i . The Schur complement S provides the correct marginal covariances by explicitly marginalizing the highly correlated pose variables, which is crucial for precise uncertainty in SLAM/VIO. Hence $\Sigma_{\text{world},i}$ captures full pose–landmark coupling, unlike the common approximation $\Sigma_{\text{world},i} \approx H_{\ell\ell,ii}^{-1}$ [22], [33].

C. Geometric Sensitivity and Conditioning

The sensitivity is obtained by conditioning the projection Jacobian via

$$\kappa(J_\pi) = \frac{\sigma_{\max}}{\sigma_{\min}}. \quad (5)$$

Here σ_{\max} and σ_{\min} correspond to the singular values obtained via SVD. A large $\kappa(J_\pi)$ indicates ill-conditioning occurring when the triangulation problem degenerates geometrically. This typically happens at grazing viewing angles or with small triangulation baselines, where small perturbations in the world pose or landmark location lead to large changes in the pixel projection, that can be interpreted as a risk due to geometrics. Depth sensitivity follows the disparity relation $\delta_z \propto 1/d^2$ reinforcing that small baselines or distant features weaken constraints. Both measures reflect the geometric amplification that result in anisotropic uncertainty.

D. Frame-Level Aggregation

Each frame t contains N_t tracked features (180–300 for EuRoC/TUM-VI, 260–300 for KITTI). The frame-level proxies are obtained via $\bar{\sigma}_t = \frac{1}{N_t} \sum_{i=1}^{N_t} \sqrt{\text{tr}(\Sigma_{\text{pixel},i})}$, $\bar{r}_t = \frac{1}{N_t} \sum_{i=1}^{N_t} \|\mathbf{r}_{\text{track},i}\|$, and $\kappa_t = \frac{1}{N_t} \sum_{i=1}^{N_t} \log(\kappa_{J,i})$, where $\mathbf{r}_{\text{track},i}$ is the reprojection residual for feature i . These aggregates reduce the ~180–300 per-feature quantities to a handful of scalars suitable for online tracking.

E. Risk Score, Normalization, and Unification

In order to derive one unified risk representation, SUPER combines the three quantities $\bar{\sigma}_t$, \bar{r}_t , and κ_t . Each component is first normalized by a z score over a sliding window (~50–100 frames):

$$\tilde{x}_t = \frac{x_t - \mu_x}{\sigma_x}, \quad (6)$$

where μ_x and σ_x denote the mean and standard deviation within the window. Clamping values to the range $[-3, 3]$ suppresses extreme transients that can arise during sudden failures. The conditioning term is further compressed using a logarithm to handle its large dynamic range. For the normalized mean uncertainty, normalized mean residual, and normalized log-conditioning denoted by $\tilde{\sigma}_t$, \tilde{r}_t , and $\tilde{\kappa}_t$, respectively, the frame-level indicators are combined to the scalar risk score r_t as follows:

$$r_t = \text{clamp}(\tilde{r}_t) + \lambda \cdot \text{clamp}(\tilde{\sigma}_t) + \text{clamp}(\log(1 + \tilde{\kappa}_t)) \quad (7)$$

The parameter $\lambda = 1.0$ controls the influence of the uncertainty. All components are z-normalized over a sliding window (50–100 frames) prior to the unification to ensure equal weighting. Hence, their magnitudes are comparable and $\lambda = 1.0$ acts as a neutral weighting that preserves this balance. After normalization, the three complementary

indicators are combined in one dimensionless scalar that reflects both measurement uncertainty and degradation.

Mapping on ISO 12100 and ISO 13849. ISO 12100 defines the risk as a proportional measure to the severity S of an event i and its probability for occurrence P :

$$R_{\text{ISO}} \propto \{S(i), P(i)\}. \quad (8)$$

SUPER provides $P(i)$ via r_t , that reflects the likelihood of estimator degradation with the propagated uncertainty, residual misfit, and geometric conditioning. Application-specific severity models $S(\cdot)$ must be provided by downstream planning layers (e.g., collision force). Since the severity is case-specific and usually corresponds to a constant value, we contend that minimizing risks is achieved by optimizing with respect to the occurrence probability P . Hence, on the basis of P , SUPER can assess the risk online. Especially, the obtained probability value can be directly mapped on ISO 13849 that defines a tolerated limit for the occurrence of dangerous events with her hour $PFDH = \frac{1}{10^6 h}$. This standard limits the rate of tolerated dangerous events to $10^6 h, \approx 114$ years. Since observing a robot application 114 years prior to commissioning is unrealistic, the probability provided by SUPER can be mapped via statistical tools as elaborated in [20]. A complete risk assessment combines both to $R_{\text{complete}}(t) = r_t \times S_{\text{application}}$.

F. Temporal Dynamics and Warning Signal

A short-horizon temporal derivative

$$\dot{r}_t = \frac{r_t - r_{t-1}}{\Delta t}, \quad (9)$$

captures rapid growth in uncertainty or residuals that result in estimator failure. Since frame-level risk can fluctuate due to benign jitter, SUPER applies a moving average on 5-10 frames to r_t prior to differentiation. This keeps the derivative responsive while suppressing noise that might produce spurious spikes [26]. In addition, a positive derivative for several consecutive frames (3–5 at 20 Hz) is required to identify a trend. By doing so, the sensitivity is reduced to isolated fluctuations. This combination provides warning signals approx. 0.3–1.0 s before feature collapse or trajectory divergence while avoiding false positives due to short transients. Alternatives like shorter moving averages or central differences produce similar behavior. SUPER refers to above formulation since it is robust and backend agnostic. In SUPER, the derivative complements the risk and serves as a temporal cue according to ISO. Application-specific severity models can be integrated at the planning or control layer.

G. Backend Integration and Computational Cost

Our framework integrates seamlessly into any factor graph optimizer that exposes Jacobians and forms a structured Hessian (Ceres [31], g2o [24], GTSAM [22]). Figure 3 shows the full VIO pipeline. All uncertainty computations refer to quantities that can be directly accessed: Jacobian blocks $\mathbf{J}_{\pi,i}$ from the linearization step and the Schur complement \mathbf{S} is extracted from matrices formed during the linear solve. Hence, no additional computations are required.

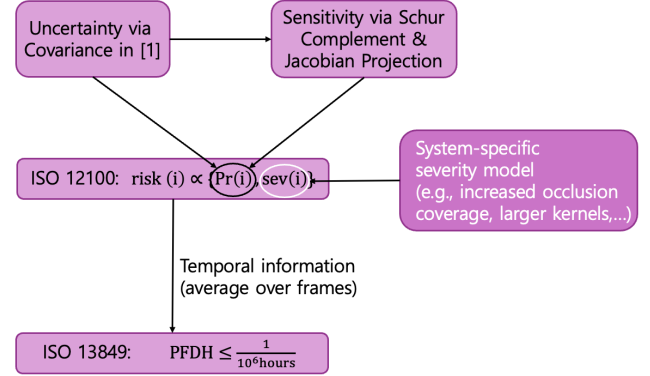


Fig. 3: **Risk score estimation.** The risk is obtained via the quantified uncertainty and sensitivity. According to ISO, the severity is application-specific. In VIO and SLAM systems, the occlusion coverage or kernel size serve as examples for the severity.

Table I reports measured overhead on a laptop CPU (AMD Ryzen 7 7735HS, 8 cores/16 threads):

TABLE I: Runtime overhead of SUPER.

Sequence	Frames	Baseline [s]	SUPER [s]	Overhead [%]
EuRoC MH.01	3 682	180.63	180.89	0.14
KITTI 00	4 541	225.58	225.61	0.013

Across both datasets, effective throughput remains at ≈ 20 Hz, and SUPER’s cost stays below 0.2% of backend optimization time on a single CPU thread.

Comparison to alternatives. Learning-based uncertainty methods (D3VO [7], DeepVO [14]) require separate neural network inference. These add 15–25% runtime cost and GPU memory. Filter-based approaches (ROVIO [8], MSCKF [2]) incur 30–50% overhead through propagation and update steps. SUPER’s <0.2% overhead represents a *two-orders-of-magnitude* reduction in computational cost while providing comparable uncertainty quantification. Algorithm 1 outlines the pipeline of SUPER as a pseudocode.

Algorithm 1 SUPER Risk Assessment

Require: Frame t , features $\{i = 1, \dots, N_t\}$, backend matrices H , Jacobians $\{J_i\}$

- 1: Compute Schur complement: $S = H_{\ell\ell} - H_{\ell p} H_{pp}^{-1} H_{p\ell}$
- 2: **for** each feature $i = 1$ to N_t **do**
- 3: $\Sigma_{\text{world},i} \leftarrow S_{ii}^{-1}$ {Extract 3×3 block}
- 4: $\Sigma_{\text{pixel},i} \leftarrow J_{\pi,i} \Sigma_{\text{world},i} J_{\pi,i}^\top$
- 5: $\kappa_{J,i} \leftarrow \sigma_{\max}(J_{\pi,i}) / \sigma_{\min}(J_{\pi,i})$ {SVD}
- 6: **end for**
- 7: $\bar{\sigma}_t, \bar{r}_t, \kappa_t \leftarrow$ aggregate via (III-D)
- 8: $r_t \leftarrow$ fuse and normalize via (7)
- 9: $r_t^{\text{smooth}} \leftarrow$ moving-average(r_t , window = 5–10)
- 10: $\dot{r}_t \leftarrow (r_t^{\text{smooth}} - r_{t-1}^{\text{smooth}}) / \Delta t$
- 11: **return** Risk indicators: $r_t^{\text{smooth}}, \dot{r}_t$, and frame proxies: $\bar{\sigma}_t, \bar{r}_t, \kappa_t$

IV. EXPERIMENTAL SETUP

The evaluation of SUPER is performed on three datasets: EuRoC MAV [34] for indoor stereo with IMU, TUM-VI [35] for visual-inertial sequences with fast motion and challenging illumination, and KITTI Odometry [36] for outdoor stereo with long trajectories and high speed.

A. Noise Injection and Uncertainty Evaluation

The evaluation covers common visual failure sources: blur, additive pixel noise, compression, downsampling, partial occlusions, and multiplicative intensity dependent noise. Each corruption is generated at several predefined severity levels (e.g., larger blur kernels, higher noise variance, stronger compression, increased occlusion coverage) and applied either to each frame of a sequence or to short temporal windows to model brief disturbances like occlusions or blur spikes. This protocol yields repeatable degradation patterns for analyzing how uncertainty and risk evolve with reduced visual quality. *Additive vs. Multiplicative Noise.* Most degradations in the evaluation, as Gaussian noise, blur, and compression are additive due to the absence of dependencies with the of image content. Speckle noise is multiplicative with variance proportional to pixel intensity that produces heteroscedastic spatially varying errors. These violate the locally uniform noise assumption of the first order propagation [28] and affect high gradient regions. The resulting residual spikes and conditioning instabilities are examined in Sec. V.

B. Pipeline, Metrics, and Baselines

Each corrupted sequence is processed by the VIO pipeline adapted from the work in Choi et al. in [12] combining FAST detection, stereo matching, triangulation, and sliding window BA with covariance extraction. This corruption protocol is also applied to ORB-SLAM3 [4]. The uncertainty is obtained from pixel covariances

$$\Sigma_{\text{pixel}} = J_{\pi} \Sigma_{\text{world}} J_{\pi}^{\top},$$

scalarized as $\sigma = \sqrt{\text{tr}(\Sigma_{\text{pixel}})}$ and averaged over features. Geometric diagnostics include Jacobian conditioning κ_J and a triangulation conditioning proxy κ_T . Additional outputs are reprojection residuals, feature counts, outlier ratio, and a pose covariance proxy. The risk indicator r_t is computed by unifying normalized uncertainty, conditioning, and residuals. SUPER is evaluated against four baselines under identical settings: (B1) VO/VIO without uncertainties [12], (B2) ORB-SLAM3 without uncertainties [4], (B3) corrupted VO/VIO, and (B4) corrupted ORB-SLAM3.

V. RESULTS

A. Experimental Scope and Joint Trends

This section evaluates SUPER on VIO and SLAM pipelines: (i) the stereo visual-inertial odometry (VIO) pipeline [12] and (ii) ORB-SLAM3 for long-horizon SLAM [4]. Corruptions cover EuRoC [34], KITTI [36], and TUM-VI [35],

including blur, pixel noise, temporal noise, occlusion, salt-pepper, speckle, JPEG/compression, and combined degradations. After removing runs with true backend failure (no convergence), the final dataset comprises

- VIO: 314 valid runs and approx. 1.0M frames (KITTI 113, EuRoC 53, TUM 148),
- SLAM: 399 valid runs and approx. 0.75M frames (KITTI 135, EuRoC 90, TUM 174).

This yields more than 700 experiments and over ten million feature-level Jacobian and uncertainty values. For SLAM, 55 EuRoC/TUM experiments at the max. occlusion or pixel-noise levels exceed the 15 min budget and are terminated. Their logs are kept to analyze early-warnings. Across EuRoC, KITTI, and TUM-VI, the risk shows consistent trends: Measurement corruptions (blur or pixel noise) lead to moderate increase while geometry corruptions (occlusion, salt-pepper, speckle) produce sharp excursions. This is significant for SLAM due to its reliance on long-horizon triangulation and keyframe connectivity. In contrast, VIO shows smaller magnitudes because of IMU priors and higher update rates.

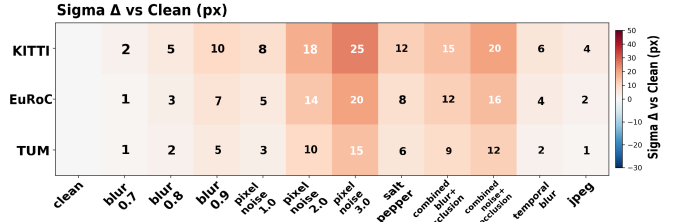


Fig. 4: Shift of mean pixel standard deviation $\bar{\sigma}$ relative to the clean baseline across datasets and corruption types. Positive values indicate inflated uncertainty compared to clean conditions.

Figure 4 illustrates these trends. The heatmap shows how the mean propagated uncertainty $\bar{\sigma}$ inflates to clean conditions across datasets and corruption types. Measurement corruptions inflate uncertainty almost monotonically. Geometric corruptions produce abrupt shifts that align with the risk excursions in SLAM. The characteristics of the data sets become visible: EuRoC's constrained indoor geometry, KITTI's long-range outdoor structure, and TUM-VI's dynamic motion. In all experiments, the risk remains tightly coupled to the propagated standard deviation. The correlation between mean σ and mean risk is $r = 0.997$ for VIO and $r = 0.932$ for SLAM. An example is shown in Figure 5.

B. Backend Behavior of VIO and SLAM

a) *VIO global sensitivity and dynamics:* VIO shows a consistent ordering in uncertainty and risk: EuRoC < KITTI < TUM-VI. This matches motion dynamics and scene depth. The pixel noise and blur increase almost linearly with the propagated covariance. Occlusion and impulse noise (salt-pepper, speckle) dominate worst-case behavior. This confirms that the propagated Jacobian information captures both measurement noise and geometric conditioning. Overall, the indicator responds to sudden changes while also reflecting accumulating degradation. Aggregated over all VIO runs, the mean risk amounts

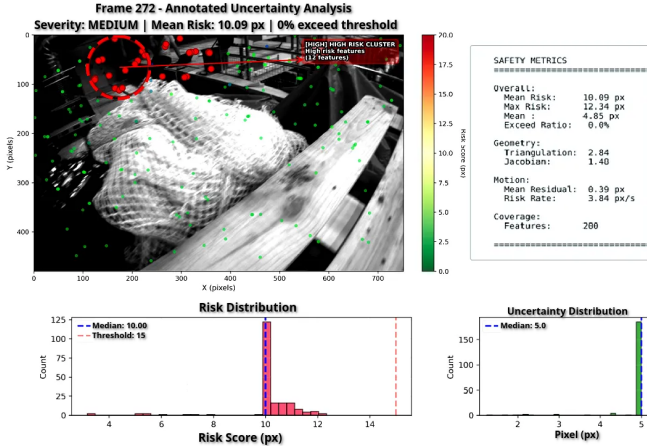


Fig. 5: **Frame level risk visualization.** Feature tracks are colored by risk. High risk clusters are highlighted. The right panel summarizes frame level safety metrics. The plots show the distributions of risk and uncertainty.

to 9.29 px (median 9.21 px) and the mean risk margin to -15.68 px. The bulk of VIO operation thus stays below the threshold with occasional short excursions above.

b) SLAM: Global behavior, corruption response, and lead time: SLAM exhibits the same corruption ordering as VIO but with broader risk distributions. The risk margin stays elevated for longer intervals and individual sequences can re-enter high risk regimes multiple times before timing out. Across all SLAM runs, strong correlations between the mean risk margin and classical cues (residuals, Jacobian conditioning, feature scarcity) can be recognized. Across both estimator families, a consistent response to increasing corruption severity is identified. Measurement noise inflates risk smoothly, while geometry corruptions produce sharp increases. SLAM shows more dominant reactions at higher severity values because the long-horizon mapping depends on stable triangulation and keyframe consistency. These trends align with the Jacobian structure. Lead time CDFs reveal that the indicator provides 0.4–1.2 s of warning before SLAM timeouts for 90% of successful runs. Quantitatively, the mean warning lead time for successful SLAM runs is 133 s (median 102 s, 90th percentile 184 s), while timeout runs yield a mean warning lead time of 7.5 s (median 0 s). Recovered SLAM sequences show how margins grow and fall back below threshold. This highlights early warnings and the possibility for recovery.

Risk threshold: For the experiments in Sec. V-C and Sec. V-C.0.c, the risk threshold r_{th} is specified as the 95th percentile of r_t over all clean frames for each dataset. This corresponds to a tolerated probability of estimator degradation in ISO 12100. The threshold is computed once from clean sequences and held fixed across all corruption conditions.

C. Detection, Prediction, and Policy Evaluation

a) Detection and safety metrics: We evaluate three risk indicators during operation: A margin criterion (risk margin

exceeding zero), a trend criterion (risk trend above a dataset-specific threshold), and a detector that triggers when one of both conditions is met. On SLAM, the margin criterion detects 98.1% of timeout runs while categorizing all successful runs as safe at the end of their sequences. The trend criterion captures 31.5% of timeouts, and the detector matches the margin performance since margin violations dominate failures. For VIO, no timeouts occur. The trend criterion detects 45.9% of successful runs with elevated temporal activity, whereas the margin criterion rarely triggers. Combining these two shows similarities with the trend-based detector. The statistics show that margin-based detection is the primary safety signal for long-horizon SLAM, while trend information highlights bursts of activity in short-horizon VIO. Under nominal conditions, the indicator remains inactive. On clean KITTI and TUM-VI runs, VIO has 0 % of frames above the threshold. On EuRoC, few high-risk states occur due to more rapidly varying motions. These events occur in short bursts (med. 1 frame, max. 35 frames). For long-horizon SLAM, clean KITTI runs show < 1 % of frames above the threshold with bursts of approx. three frames. EuRoC and TUM-VI SLAM logs stay above the threshold almost continuously. This matches the different observability properties of VIO and SLAM and indicates that the indicator only is triggered in necessary cases, like latent drifts in SLAM.

b) Predictive power for near-future degradation: Instantaneous risk shows limited correlation with cumulative trajectory error. This behavior is expected since trajectory-level RMSE accumulates over hundreds of frames. We therefore evaluate whether risk indicators predict impending degradation over a finite horizon. For each frame t , a degradation event is defined as a trajectory error exceeding 1.0 m within the next $N = 50$ frames (2.5 s at 20 Hz). Table II reports AUC values for predicting these events across all 314 VIO runs (811,507 frames). Varying the horizon between 25 and 100 frames and the error threshold between 0.5 m and 2.0 m does not induce significant variations on the absolute AUC values. The relative ranking between indicators remains.

TABLE II: Predictive power for future degradation events. $N = 50$ frames ahead, error threshold 1.0 m, 314 VIO runs, 811K frames.

Indicator	AUC	vs. Chance
Mean risk (ours)	0.585	+17%
Mean sigma (ours)	0.582	+16%
Mean residual	0.490	≈ 0%
Feature count	0.193	-61%
Jacobian condition	0.190	-62%

The uncertainty-based indicators achieve $AUC \approx 0.58$, thereby outperforming classical heuristics. Mean residuals ($AUC = 0.49$) perform at chance level while feature count and Jacobian conditioning ($AUC \approx 0.19$) are anti-correlated with future degradation. This effect occurs because challenging scenes underlie more features (dense texture) and better conditioning (close-range tracking) yet still degrade due to dynamic motion, blur, or occlusion. These are cap-

tured by the propagated uncertainty but cannot be captured solely by geometric proxies. The improvement of $\approx 20\%$ over residuals (0.585 vs. 0.490) demonstrates that SUPER provides insights on impending failure that is not visible in the reprojection error.

Hazard curve analysis: To interpret the risk, we stack r_t into deciles and compute the probability of violating the 1 m translation error bound within the subsequent 50 frames. The resulting hazard curve shows that the lowest risk decile (mean $r_t \approx 5.8$ px) fails in 2.3 %, whereas mid-range risk values (mean $r_t \approx 9.2$ px) correspond to $\approx 35\%$ failure probability. The highest risk decile reaches $\approx 45\%$. These results confirm the accuracy of SUPER for estimating the failure probability, and thus risks according to ISO 12100. We note that even the complete knowledge on the actual frame limits the prediction of future degradation because failures depend on the subsequent motion and scene conditions that are difficult to estimate. The partial observability of the task limits the accuracy of the risk estimation. One possibility to study the quality of the risk estimation lies in the ROC AUC estimation. Basically, the AUC expresses a model’s ability to distinguish between classes: AUC=1.0 indicates a perfect classifier while AUC=0.5 equals random decision making. For SUPER, AUC describes whether a randomly selected failing frame receives a higher score than a randomly selected frame without failures. The obtained AUC values of 0.6 hint at a more reliable classifier compared to the baseline (AUC = 0.49).

c) Decision policy evaluation for SLAM: Additionally, we evaluate a straightforward stop/relocalization policy on 399 SLAM runs. Here, caution shall be triggered when risk remains elevated above a sequence-specific threshold for K consecutive frames. Table III reports detection performance across threshold values. A $K = 10$ frame (0.5 s) persistence requirement achieves 89% recall with 8.4% false positive rate (precision 62.8%). This provides sufficient warning time: In our experiments, 0.5–1.0 s is sufficient to decelerate a MAV or trigger relocalization before catastrophic drift.

TABLE III: SLAM stop/relocalization policy performance. 399 SLAM runs, 55 timeouts. \star = recommended configuration.

Threshold (frames)	Recall	FPR	Precision
5	69.1%	8.4%	56.7%
10 \star	89.1%	8.4%	62.8%
20	92.7%	25.6%	36.7%
30	92.7%	25.6%	36.7%
60	92.7%	29.9%	33.1%
120	96.4%	53.8%	22.3%

Shorter thresholds ($K = 5$) exhibit lower recall (69%) and miss failures that develop gradually. Longer thresholds ($K \geq 20$) inflate false positives ($FPR > 25\%$), triggering unnecessary stops during transient uncertainty spikes that resolve naturally. This shows how uncertainty propagation enables to balance safety (high recall) with high efficiency (low false positives).

d) Ablation Studies and Contribution of Indicators: The risk combines the propagated pixel uncertainty $\bar{\sigma}$, average reprojection residual \bar{r} , and Jacobian conditioning κ . To quantify the individual contribution of each mode, we perform an ablation study on VIO and SLAM. Since the frame-level ground truth is available for VIO, frame-wise AUC values are averaged over all runs. For SLAM, frame-level ground truth is not available. We treat each run as a single sample and consider the timeout as the target. Each indicator is converted to a score on run-level: Delta uncertainty $\Delta\bar{\sigma}$, delta residual $\Delta\bar{r}$, mean conditioning κ , and the negated warning lead time (shorter lead at higher risk). Table IV shows the results.

TABLE IV: AUC for VIO frame errors and SLAM timeouts.

Indicator	AUC (VIO)	AUC (SLAM)
Sigma only ($\bar{\sigma}$)	0.563	0.946
Residual only (\bar{r})	0.416	0.566
Conditioning only (κ)	0.489	0.609
Risk margin	0.536	0.989

The results match the expected behavior: VIO rarely enters long-lasting degeneracy. Hence, measurement noise dominates its local error, thereby making $\bar{\sigma}$ the strongest single cue. SLAM fails through geometry collapse and accumulated drift making conditioning and lead time more informative. The risk achieves the highest AUC on SLAM and remains competitive on VIO that confirms that the indicators are complementary. Combining them enhances the reliability of warning signals.

e) Summary: Across EuRoC, KITTI, and TUM-VI, the proposed uncertainty propagation and risk reliably capture both measurement noise inflation and geometrical degeneracy. The indicators remain inactive on clean KITTI and TUM-VI sequences while short bursts on clean EuRoC reflect the dataset’s dominant motion variations. Risk correlates strongly with upcoming failures: Future prediction AUC reaches ≈ 0.58 compared to ≈ 0.49 for residuals. The hazard curve shows failure probabilities rising from 2 % in the lowest risk decile to approx. 45 %. The margin-based stop policy catches nearly all SLAM timeouts. VIO’s trend signals expose short-term bursts without false alarms. We conclude that the indicator acts as a calibrated, backend-agnostic measure for the probability of short time future degradation while preserving real-time performance.

VI. DISCUSSION AND LIMITATIONS

The results show that the first order uncertainty propagation is reliable in the small residual regime characteristic of modern VIO. Under pixel noise, blur, and compression, the propagated uncertainty grows with the severity. This reflects the frequent relinearization and dense feature support that these systems rely on. With decreasing geometry, the occlusion, weak parallax and low texture must be additionally considered. These push the normal equations toward ill conditioning, where the Jacobian conditioning and residuals respond sharply. Combining these indicators

with short horizon temporal trends separates measurement noise from geometric collapse, and yield strong detection of failure modes. Furthermore, data set specific patterns are identified. EuRoC produces the lowest uncertainty followed by KITTI and TUM VI. Corruption injections cause minor changes, while occlusion and combined degradations yield major risks. The risk's temporal derivative provides warning signals of degradation. Here, spikes precede large residual bursts or feature collapse by hundreds of milliseconds with negligible computational cost. SUPER's limitations become visible under extreme corruptions, where feature support vanishes and the information matrix becomes singular.

VII. CONCLUSION

We presented the sensitivity-based uncertainty evaluation framework SUPER for VO,VIO and SLAM that derives interpretable risk indicators with real time performance by exploiting the computations in the backend optimization. Across EuRoC, KITTI, and TUM-VI, SUPER achieves (i) reliable uncertainty estimates under measurement noise, (ii) robust warning signals for geometry-driven failures, and (iii) strong detection of mixed indicators. The additional computational costs stay below 0.2%. The results remain consistent for VIO and SLAM and indicate that the risk emerges from the Jacobian. The findings emphasize the importance of estimating risks in VO,VIO and SLAM. The limited correlation between the risks and the cumulative trajectory error matches theoretical expectations. SUPER predicts degradation 2.5 s in advance with 89% recall and an 8% false positive rate, thereby enabling risk-aware online decision-making. Future work will extend SUPER to heteroscedastic uncertainties and long-horizon SLAM.

ACKNOWLEDGMENT

The authors thank Seungwon Choi for fruitful discussions, invaluable feedback and for providing the codebase in [12] that served as a foundational basis for our research.

REFERENCES

- [1] A. J. Davison *et al.*, “Monoslam: Real-time single camera slam,” *IEEE Trans. Pattern Anal. Mach. Intell.*, vol. 29, no. 6, pp. 1052–1067, 2007.
- [2] A. I. Mourikis and S. I. Roumeliotis, “A multi-state constraint kalman filter for vision-aided inertial navigation,” in *ICRA*, 2007, pp. 3565–3572.
- [3] S. Leutenegger *et al.*, “Keyframe-based visual–inertial odometry using nonlinear optimization,” *Int. J. Robotics Research*, vol. 34, no. 3, pp. 314–334, 2015.
- [4] C. Campos *et al.*, “Orb-slam3: An accurate open-source library for visual, visual–inertial, and multi-map slam,” *IEEE Transactions on Robotics*, vol. 37, no. 6, pp. 1874–1890, 2021.
- [5] Z. Teed and J. Deng, “Droid-slam: Deep visual slam for monocular, stereo, and rgb-d cameras,” in *NeurIPS*, 2021.
- [6] D. Hendrycks and T. Dietterich, “Benchmarking neural network robustness to common corruptions and perturbations,” in *ICLR*, 2019, arXiv:1903.12261.
- [7] N. Yang *et al.*, “D3VO: Deep depth, deep pose and deep uncertainty for monocular visual odometry,” in *CVPR*, 2020, pp. 1281–1292.
- [8] M. Bloesch *et al.*, “Iterated extended kalman filter based visual–inertial odometry using direct photometric feedback,” *Int. J. Robotics Research*, vol. 36, no. 10, pp. 1053–1072, 2017.
- [9] C. Stachniss, J. J. Leonard, and S. Thrun, “Simultaneous localization and mapping,” in *Springer Handbook of Robotics*, 2nd ed., B. Siciliano and O. Khatib, Eds. Springer, 2016, pp. 1153–1176.
- [10] P. A. Lasota, T. Fong, and J. A. Shah, “A survey of methods for safe human-robot interaction,” *Foundations and Trends in Robotics*, vol. 5, no. 4, pp. 261–349, 2017.
- [11] International Organization for Standardization, “ISO 12100:2010 Safety of machinery – General principles for design – Risk assessment and risk reduction,” <https://www.iso.org/standard/51528.html>, 2010, ISO Standard.
- [12] S. Choi *et al.*, “Statistical uncertainty learning for robust visual–inertial state estimation,” *arXiv preprint arXiv:2510.01648*, 2025.
- [13] T. Shan and B. Englot, “Lio-sam: Tightly-coupled lidar inertial odometry via smoothing and mapping,” in *IROS*, 2020.
- [14] S. Wang *et al.*, “Deepvo: Towards end-to-end visual odometry with deep recurrent convolutional neural networks,” in *ICRA*, 2017, pp. 2043–2050.
- [15] B. Wagstaff, E. Wise, and J. Kelly, “A self-supervised, differentiable kalman filter for uncertainty-aware visual–inertial odometry,” in *IEEE/ASME Int. Conf. Adv. Intell. Mechatron. AIM*, 2022, pp. 1388–1395.
- [16] L. Blackmore, M. Ono, and B. C. Williams, “Chance-constrained optimal path planning with obstacles,” *IEEE Trans. Robotics*, vol. 27, no. 6, pp. 1080–1094, 2011.
- [17] J. A. Gaus *et al.*, “Guard: Toward a compromise between traditional control and learning for safe robot systems,” *arXiv preprint arXiv:2509.23312*, 2025.
- [18] W.-J. Baek and T. Kröger, “Safety evaluation of robot systems via uncertainty quantification,” 02 2023.
- [19] W.-J. Baek *et al.*, “Combining measurement uncertainties with the probabilistic robustness for safety evaluation of robot systems,” in *IROS*, 2023, pp. 473–480.
- [20] W.-J. Baek, “Uncertainty quantification and sensitivity-based optimization methods for robot systems,” Ph.D. dissertation, Karlsruher Institut für Technologie (KIT), 2024.
- [21] S. Sánchez and K. Otto, “Uncertainty quantification and reduction using jacobian and hessian information,” *Design Science*, vol. 7, p. e20, 2021.
- [22] F. Dellaert, “Factor graphs and gtsam: A hands-on introduction,” Georgia Institute of Technology, Tech. Rep. GT-RIM-CP&R-2012-002, 2012.
- [23] M. Kaess *et al.*, “isam2: Incremental smoothing and mapping using the bayes tree,” *The International Journal of Robotics Research*, vol. 31, no. 2, pp. 216–235, 2012.
- [24] R. Kümmerle *et al.*, “g2o: A general framework for graph optimization,” in *ICRA*, 2011, pp. 3607–3613.
- [25] T. D. Barfoot, *State Estimation for Robotics*. Cambridge University Press, 2017.
- [26] S. Thrun, W. Burgard, and D. Fox, *Probabilistic Robotics*. MIT Press, 2005.
- [27] G. P. Huang, A. I. Mourikis, and S. I. Roumeliotis, “Observability-based rules for designing consistent ekf slam estimators,” *The International Journal of Robotics Research*, vol. 29, no. 5, pp. 502–528, 2010.
- [28] A. Kendall and Y. Gal, “What uncertainties do we need in bayesian deep learning for computer vision?” in *NeurIPS*, 2017.
- [29] E. Ilg *et al.*, “Uncertainty estimates and multi-hypotheses networks for optical flow,” in *Proc. European Conf. on Computer Vision*, 2018, pp. 652–667.
- [30] L. De Vito *et al.*, “Sensitivity analysis of a visual inertial odometry-based navigation system for uav,” in *I2MTC*, 2025, pp. 1–6.
- [31] S. Agarwal, K. Mierle, and Others, “Ceres solver,” *Journal of Open Source Software*, vol. 7, no. 74, p. 3735, 2022.
- [32] B. Triggs *et al.*, “Bundle adjustment A modern synthesis,” in *Vision Algorithms: Theory and Practice*, ser. Lecture Notes in Computer Science. Springer, 2000, vol. 1883, pp. 298–372.
- [33] M. Kaess, A. Ranganathan, and F. Dellaert, “iSAM: Incremental smoothing and mapping,” *IEEE Transactions on Robotics*, vol. 24, no. 6, pp. 1365–1378, 2008.
- [34] M. Burri *et al.*, “The EuRoC micro aerial vehicle datasets,” *The International Journal of Robotics Research*, vol. 35, no. 10, pp. 1157–1163, 2016.
- [35] D. Schubert *et al.*, “The TUM-VI benchmark for evaluating visual–inertial odometry,” *IEEE RAL*, vol. 3, no. 3, pp. 2637–2644, 2018.
- [36] A. Geiger, P. Lenz, and R. Urtasun, “Are we ready for autonomous driving? the KITTI vision benchmark suite,” in *CVPR*, 2012, pp. 3354–3361.